JOURNAL OF SYNCHROTRON RADIATION
ISSN 1600-5775

Interaction of a relativistic dense electron beam with a laser wiggler in a vacuum: self-field effects on the electron orbits and free-electron laser gain

E. Abbasi, S. Jafari* and R. Hedayati

Department of Physics, University of Guilan, Rasht 41335-1914, Iran. *Correspondence e-mail: sjafari@guilan.ac.ir

Received 23 January 2016
Accepted 4 August 2016

Edited by G. Grübel, HASYLAB at DESY, Germany

Keywords: dense electron beam; laser wiggler; self-fields; stability analysis; free-electron laser.

Employing laser wigglers and accelerators provides the potential to dramatically cut the size and cost of X-ray light sources. Owing to recent technological developments in the production of high-brilliance electron beams and high-power laser pulses, it is now conceivable to make steps toward the practical realisation of laser-pumped X-ray free-electron lasers (FELs). In this regard, here the head-on collision of a relativistic dense electron beam with a linearly polarized laser pulse as a wiggler is studied, in which the laser wiggler can be realised using a conventional quantum laser. In addition, an external guide magnetic field is employed to confine the electron beam against self-fields, therefore improving the FEL operation. Conditions allowing such an operating regime are presented and its relevant validity checked using a set of general scaling formulae. Rigorous analytical solutions of the dynamic equations are provided. These solutions are verified by performing calculations using the derived solutions and well known Runge–Kutta procedure to simulate the electron trajectories. The effects of self-fields on the FEL gain in this configuration are estimated. Numerical calculations indicate that in the presence of self-fields the sensitivity of the gain increases in the vicinity of resonance regions. Besides, diamagnetic and paramagnetic effects of the wiggler-induced self-magnetic field cause gain decrement and enhancement for different electron orbits, while these diamagnetic and paramagnetic effects increase with increasing beam density. The results are compared with findings of planar magnetostatic wiggler FELs.

1. Introduction

The free-electron laser (FEL) has been demonstrated to be a tunable source of high-power radiation over the wide range of the electromagnetic spectrum by using a relativistic electron beam passing over an undulating magnetic field called a wiggler. Considerable efforts have been made to operate FELs at shorter wavelengths and higher powers (Ackermann *et al.*, 2007; McNeil & Thompson, 2010; Ribic & Margaritondo, 2012; Ishikawa *et al.*, 2012; Tiedtke *et al.*, 2009; Allaria *et al.*, 2015; Harmand *et al.*, 2013; Yabashi *et al.*, 2015; Wu *et al.*, 2012; Lehmkühler *et al.*, 2014). In this regard, many proposed X-ray FELs (with a wavelength range from a few nanometers down to a few angstroms) have been designed to generate radiation starting from the shot noise of an e-beam, the so-called SASE (self-amplified spontaneous emission) mechanism (see Margaritondo & Ribic, 2011, and references therein). The main drawbacks of the SASE-FEL are (i) a long conventional wiggler is required, (ii) there is a relatively high level of shot-to-shot fluctuations, and (iii) relatively poor longitudinal coherence. Thus, a number of alternative concepts are under consideration such as seeding with a coherent signal and

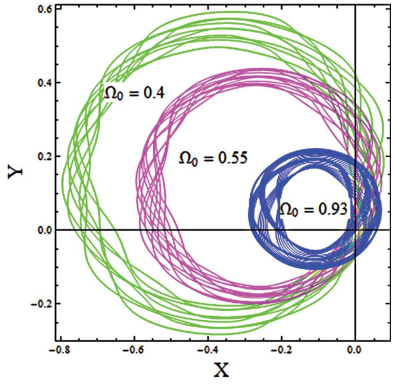

prebunching the e-beam prior to injection into the wiggler (Geloni *et al.*, 2011; Allaria *et al.*, 2012; Amann *et al.*, 2012; Ratner *et al.*, 2015; Svitozar *et al.*, 2015; Svitozar, 2016; Parmigiani & Ratner, 2016). One way of generating short wavelengths is to employ a laser pulse as a wiggler, instead of the static wiggler used in the planned classical SASE experiments (Zholents, 2005; Fuchs *et al.*, 2009; Polyanskiy *et al.*, 2011; Dattoli *et al.*, 2012, 2015).

The basic difference between conventional magnetic and laser wigglers lies in the frequency of the output radiation. In a conventional FEL, electrons propagate in the magnetostatic wigglers characterized by a period λ_w, and by a strength parameter $K_w = eB_w\lambda_w/2\pi mc$, where m and e are the electron mass and charge, respectively, c is the speed of light and B_w is the peak magnetic field. In conformity with the resonance relation in such a FEL, $\lambda_r \cong \lambda_w(1 + K_w^2)/2\gamma^2$, the output wavelength of the radiation λ_r can be decreased by reduction of the wiggler wavelength λ_w or by increasing the e-beam energy γ. Owing to technical limitations of the wiggler wavelength ($\lambda_w \geq 1$ cm) and magnetic field strength (*e.g.* in a helical wiggler <50 kG), to produce a short wavelength a conventional FEL requires an e-beam with a very high γ, of the order of multi-GeV, and a wiggler length of a few tens of meters (Freund & Antonsen Jr, 1992). In this regard, laser-pumped FELs proposed since the Doppler upshift for such a pump laser were a factor of two higher than magnetostatic wigglers with comparable periods. In other words, the wavelength of radiation for a laser wiggler with period λ_1 scales as (Dattoli *et al.*,1999)

$$\lambda_r \cong \frac{\lambda_1}{4\gamma^2}\left(1 + \frac{K_1^2}{2}\right), \tag{1}$$

where the strength parameter, associated with the laser-wiggler intensity I_1, in practical units reads as

$$K_1 \cong \left(2.3 \times 10^{-5}\, \lambda_1^2\,[\mathrm{cm}^2]\; I_1\,[\mathrm{MW\,cm^{-2}}]\right)^{1/2}. \tag{2}$$

In comparison with the conventional wigglers, laser-pulse wigglers have a very small period (~μm) and therefore produce shorter-wavelength free-electron radiation with lower electron energies; the construction of long wigglers can also be avoided. Laser-pumped FELs also offer a more convenient continuous tunability, by changing the laser frequency (Fuchs *et al.*, 2009; Polyanskiy *et al.*, 2011; Dattoli *et al.*, 2012). An infrared laser pulse, coming from a high-power Nd or CO_2 laser with wavelength of 1–10 μm, could yield FEL radiation in the tens of nanometers range with electrons of only a few MeV (Kawamura *et al.*, 2000; Gordon *et al.*, 2001; Bacci *et al.*, 2006; Petrillo *et al.*, 2008). Besides, such a FEL might provide the opportunity to observe quantum mechanical effects in FEL operation, which in the conventional designs do not play any role (Bonifacio, 2005; Bonifacio *et al.*, 2007).

Important experimental and theoretical attempts have been made to obtain a set of reference quantities, useful for understanding the feasibility of the laser-pumped X-ray FEL. For example, the energy dispersion of the electrons should be less than $1/\rho$, where ρ is the FEL Pierce parameter (Bonifacio *et al.*, 1984). Therefore, this scheme would require a high-quality monoenergetic e-beam, together with the requirement of constancy of the laser intensity along the interaction region. Owing to these major issues, a laser-wiggler FEL was viewed for long time as an interesting curiosity because the achievable laser intensity did not guarantee radiation growth and saturation. This possibility has been reconsidered, as high-power lasers have undergone a spectacular evolution. A record intensity of 2×10^{26} W m^{-2} has been obtained (Yanovsky *et al.*, 2008), and the upcoming petawatt lasers aim at intensities of the order of 10^{27} W m^{-2} (Norby *et al.*, 2005). In the near future, intensities of the order of 10^{28}–10^{30} W m^{-2} are foreseen at the Extreme Light Infrastructure (ELI) (Mourou & Tajima, 2011). The present-day technology is therefore mature enough to conceive the experimental programs aiming at the realisation of a laser-pumped X-ray FEL.

In a FEL, apart from such parameters as the magnetic field strength or wavelength, polarization is one of the most important characteristics of the wiggler. Like magnetostatic wigglers, two types of polarization can be considered for electromagnetic wigglers: linear and circular. In most papers that have considered employing electromagnetic waves as a wiggler in FELs, a circular polarized laser is used. There are many difficulties extracting such a laser, while a linear polarized laser can be achieved using a conventional quantum laser.

Although a great deal of attention has been focused on the laser-pumped FEL configuration in recent years, most treatments heretofore have neglected the influence of the equilibrium self-fields of the electron beam, especially in the FELs with a linearly polarized laser wiggler (Bacci *et al.*, 2006; Mehdian *et al.*, 2008; Sprangle *et al.*, 2009; Olumi *et al.*, 2011; Hasanbeigi *et al.*, 2010; Jafari *et al.*, 2014; Hedayati *et al.*, 2015; Amri & Mohsenpour, 2016). It is known that space-charge effects are important in Raman FELs which operate at high electron density and low (relativistic) energy. With the present trend towards application of increasingly high current in FELs, it is of interest to consider the effects of the self-fields. The electron beam and therefore the self-field can exhibit a complex structure at the entrance to the wiggler. The self-fields can have a considerable effect on the equilibrium orbits, and can produce chaos in FELs particularly in the vicinity of gyroresonance (Bourdier & Michel-Lours, 1994). The self-fields can either enhance or reduce the external pump field, depending on the latter's phase velocity and strength of the longitudinal guide magnetic field (Kho & Lin, 1988). Hafizi & Roberson (1996) found that self-fields tend to reduce the spread in the axial velocity of the beam electrons, *i.e.* self-fields effectively cool the beam.

In this present work, we are motivated to investigate the self-field effects on the electron orbits and gain in a FEL driven by a uniform linearly polarized laser pulse (pump wave) accompanied by an axial guide magnetic field, where the pump wave is a fast laser wave propagating counter to the electron beam. In §2 we study the conditions under which FELs can be operated in the X-ray region by employing an intense laser wave as wiggler. In §3 a self-magnetic field generated by the wiggler-induced transverse velocity is found

by the self-consistent method and the equations of steady-state orbits of the electron are obtained. Moreover, a fourth-order Runge–Kutta method is employed to study the electron trajectories under the influence of the axial guide magnetic field and self-field. Derivation of the gain equation, considering the interaction of an electron with the electromagnetic radiation field, is presented in §4. In §5 a detailed numerical calculation is presented. §6 contains a conclusion and summary of the work. The stability of electron orbits in this configuration is also studied in Appendix *A*.

2. Physical model

In a laser-pumped X-ray FEL an intense-laser field replaces the magnetic wiggler field of a conventional FEL. To generate coherent X-rays with this mechanism a number of physics and technology issues must be addressed. Foremost among these are the stringent requirements placed on the electron beam quality and brightness as well as on the pump laser. In this section we introduce well known concepts and parameters, worked out in analysis of the electron back-scattering of the intense-laser wiggler, to realise general considerations on feasibility criteria of the laser-wiggler-based FELs.

The scaling laws reported in the literature (Fuchs *et al.*, 2009; Polyanskiy *et al.*, 2011; Dattoli *et al.*, 2012, 2015) can be used to derive practical formulae yielding the conditions to be satisfied by the wave-laser intensity and e-beam qualities to guarantee a reliable operation. The FEL radiation growth rate and saturation are ruled by the so-called Pierce parameter, which can be cast in the following form (Bonifacio *et al.*, 1984),

$$\rho \cong \frac{8.36\times10^{-3}}{\gamma}\left(J\,[\mathrm{A\,m^{-2}}]\,\lambda_l^2\,[\mathrm{m^{-2}}]\left\{K_1 f_b(K_1)\right\}^2\right)^{1/3}, \quad (3)$$

where $f_b(K_1)$ is defined in terms of Bessel functions as $f_b(K_1) = J_0[K_1^2/(4+2K_1^2)] - J_1[K_1^2/(4+2K_1^2)]$, and J is the e-beam current density. The saturation length, *i.e.* the wiggler length necessary to reach saturation, reads as

$$z_s \cong \lambda_1/\rho. \quad (4)$$

The operation around 50 Å, with a high density power laser of the order of 10^{14} MW cm^{-2}, requires ρ values around 10^{-3} (Grüner *et al.*, 2007). In correspondence of this value, we have assumed an e-beam current density of 10^{13} A m^{-2}. A maximum current of 10^3 A implies, therefore, an e-beam cross section S of 10^{-10} m^2. This last value, along with the saturation length, can be exploited to evaluate the laser-wiggler energy provided by Dattoli *et al.* (1999),

$$\xi = \frac{I_l S z_s}{c}. \quad (5)$$

A graph of the laser-wiggler energy ξ requirement *versus* laser-wiggler intensity I_l is plotted in Fig. 1.

This configuration puts a stringent requirement on the emittance because the radius of the e-beam that is matched to the wiggler depends on the e-beam emittance. Moreover, the condition on the emittance (Dattoli *et al.*, 2012),

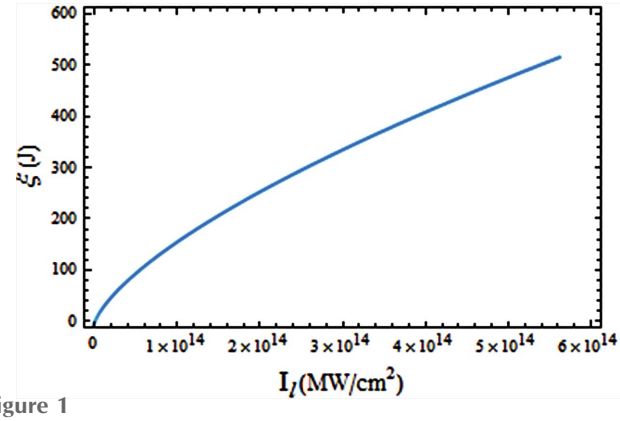

Figure 1
Graph of the laser-wiggler energy ξ requirement *versus* laser-wiggler intensity I_l. The chosen parameters are $J = 10^{13}$ A m^{-2}, $S = 10^{-10}$ m^2, $\lambda_l = 1$ µm and $\gamma = 25$.

$$\varepsilon\,[\mathrm{m\,rad}] \leq 8\times10^{-12}\lambda_r\,\text{Å}, \quad (6)$$

ensures overlapping between electrons and photons. In Fig. 2, we plot the upper limit [according to equations (1), (2) and (6)] of the normalized emittance ($\varepsilon_n = \gamma\varepsilon$) *versus* the laser-wiggler intensity I_l. The laser-wiggler intensity of 10^{14} MW cm^{-2} shows a normalized e-beam emittance of 10^{-2} mm mrad, two orders of magnitude below the best obtained values. We can expect that progress in the cathode technologies, yielding emittance improvement of one order of magnitude, may allow the possibility of using such a laser wiggler in the region above 50 Å.

The ρ parameter can be expressed in terms of the small-signal gain coefficient g as

$$\rho = \frac{1}{4N}\left(\frac{g}{\pi^2}\right)^{1/3}, \quad (7)$$

where N is the number of wiggler periods. Furthermore, for wigglers with constant parameters, the FEL saturated power is about ρ times the electron beam power (*i.e.* $P_{FEL} \cong \rho P_E$). The small-signal gain coefficient and the e-beam power are linked by

$$gI_s = \frac{1}{2N}P_E, \quad (8)$$

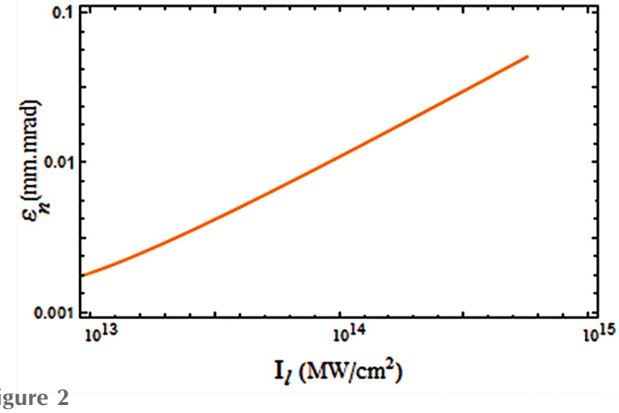

Figure 2
Graph of the optimum normalized emittance ε_n *versus* laser-wiggler intensity I_l. The chosen parameters are $\lambda_l = 1$ µm and $\gamma = 25$.

where I_s is the FEL saturation intensity (Dattoli *et al.*, 1993) and is defined by

$$I_s\,[\mathrm{MW\,cm^{-2}}] = 6.9 \times 10^2 \left(\frac{\gamma}{N}\right)^4 \left\{\frac{1}{\lambda_1\,[\mathrm{cm}]\,K_1 f_b(K_1)}\right\}. \quad (9)$$

Therefore, the FEL power can be expressed as

$$P_{\mathrm{FEL}}\,[\mathrm{MW\,cm^{-2}}] = (2/\pi)(4\pi)^3(\rho N)^4\, I_s\,[\mathrm{MW\,cm^{-2}}]. \quad (10)$$

According to equation (4), by assuming that the length of the wiggler coincides with the saturation length (*i.e.* $z_s = N\lambda_1$) we find

$$\rho N \cong 1. \quad (11)$$

This condition provides a universal link between FEL output power and saturation intensity in the following form,

$$P_{\mathrm{FEL}}\,[\mathrm{MW\,cm^{-2}}] = 1.26 \times 10^3\, I_s\,[\mathrm{MW\,cm^{-2}}]. \quad (12)$$

With the aid of equations (2), (3) and (9), as shown in Fig. 3, the expected SASE-FEL output power driven by a laser wiggler with period λ_1 (*e.g.* of the order of 1 µm) will be achieved.

As the electron beam develops a periodic microbunching, the longitudinal space-charge field between electrons tends to counteract the bunching process (Milton *et al.*, 2001). In order to analyse the focusing effects, we consider a high intensity current e-beam focused on a very small section for a length of 1 mm. Even though this is a small distance, the Coulomb repulsion forces may induce defocusing effects, which may dilute the effective current density. Hence, the e-beam in a long wiggler channel, expanding its size in free space, should be properly focused to keep the beam size nearly constant for the effective FEL interaction. There are two types of focusing: 'natural' focusing (used in many low- and medium-energy FELs) and 'strong' focusing (commonly used in X-ray FELs) (Huang & Kim, 2007). The natural focusing is due to the intrinsic property of the periodic nature of the wiggler magnetic field. It is usually too weak to be effective for the high-energy electrons that drive an X-ray FEL. Thus, a quadrupole, as a guide field, is inserted into the FEL to provide the necessary strong focusing.

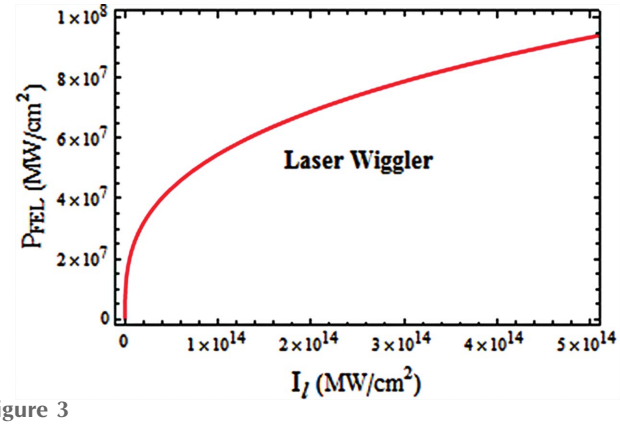

Figure 3
Graph of the SASE-FEL output power P_{FEL} *versus* laser-wiggler intensity I_l. The chosen parameters are $J = 10^{13}$ A m^{-2}, $\lambda_l = 1$ µm and $\gamma = 25$.

Typical FEL amplifiers employ an e-beam that is matched to the wiggler so that the envelope remains constant throughout the wiggler. Lawson's expression for the evolution of the r.m.s. envelope in the paraxial limit (Reiser, 1994),

$$\sigma'' = -k_q^2\sigma + \frac{\varepsilon_n^2}{\gamma^2\sigma^3} + \frac{\eta}{\gamma^3\sigma}, \quad (13)$$

can be exploited to have an idea of the defocusing due to the charge contributions. We have denoted by σ the r.m.s. e-beam transverse section and with σ'' the second derivative with respect to the longitudinal coordinate. Furthermore, ε_n is the r.m.s. emittance of the e-beam and the beam perveance $\eta = I/2I_A$ controls the effect of the space-charge contribution with the Alfven current $I_A = ec/r_e \cong 17$ kA. The quadrupole focusing gradient k_q is

$$k_q = \frac{eB_0}{2\gamma m_e c} = \frac{a_0}{\sqrt{2}\gamma}\, k_0, \quad (14)$$

where $k_0 = 2\pi/\lambda_0$ is the quadrupole wavenumber and $a_0 = eB_0/\sqrt{2}k_0 m_e c$ is the dimensionless quadrupole strength parameter corresponding to the peak on-axis field B_0.

The results of the r.m.s. beam size analysis are given in Fig. 4, from which it is evident that the charge defocusing effect is by no means negligible even over the 1 mm interaction length. In this region the e-beam transverse dimensions do not grow significantly, while its divergence grows from 10^{-5} to 10^{-3} rad.

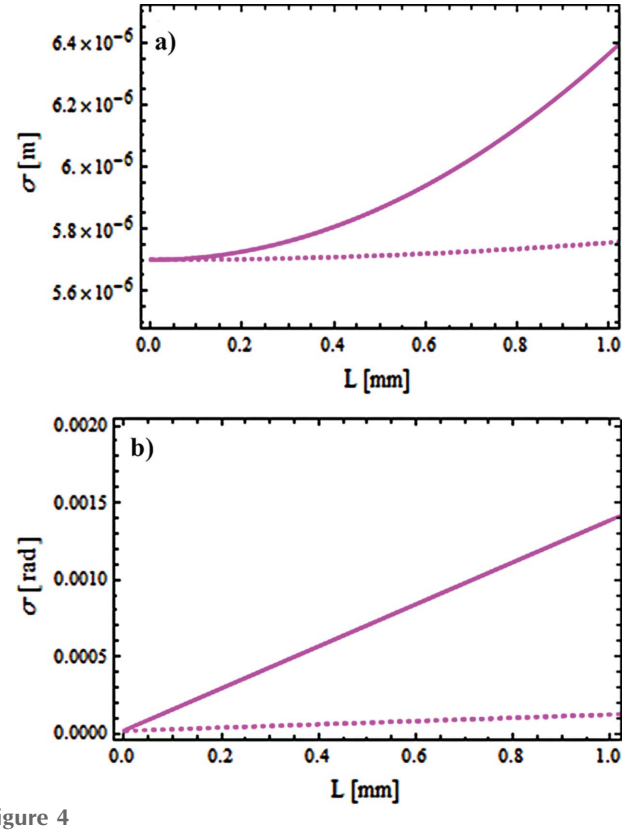

Figure 4
Graph of the e-beam envelope (*a*) and the e-beam divergence (*b*) *versus* the longitudinal coordinate for $\gamma = 25$, $I = 1$ kA, $\varepsilon_n = 10^{-2}$ mm mrad and $k_q = 10$ m^{-1}. The dotted line refers to the case in which the space-charge effects have not been included.

Thereby, a guiding field is necessary in the FEL to restrict the electrons against the radial space-charge forces over a reasonable length region. A high density power laser can be, therefore, a good candidate for a laser wiggler to support the SASE-FEL operation.

3. Single-particle trajectories

The dynamics of FEL operation with magnetostatic or laser wigglers is essentially the same, if we limit ourselves to modest electron energies and not too short laser wavelengths, in order to avoid quantum corrections.

The specific configuration we consider is that of a relativistic electron beam propagating through an axial guide magnetic field, $\mathbf{B}_0$ ($= B_0\hat{e}_z$), and an antiparallel propagating linearly polarized laser wiggler characterized in terms of amplitude, wavenumber and frequency, B_l, k_l and ω_l, as

$$\mathbf{E}_\mathrm{l} = -\frac{\omega_\mathrm{l}}{ck_\mathrm{l}} B_\mathrm{l} \sin(k_\mathrm{l}z + \omega_\mathrm{l}t)\hat{e}_x, \tag{15}$$

$$\mathbf{B}_\mathrm{l} = B_\mathrm{l} \sin(k_\mathrm{l}z + \omega_\mathrm{l}t)\hat{e}_y. \tag{16}$$

In order to model the self-fields, we make the assumption of a uniform electron density profile $n_\mathrm{b}(r) = n_\mathrm{b}$ = constant for $r \le r_\mathrm{b}$ and $n_\mathrm{b}(r) = 0$ for $r > r_\mathrm{b}$, where n_b is the number density of the electrons and r_b is the radius of the beam. The beam equilibrium self-electric field induced by steady-state charge density of the non-neutral electron beam can be obtained by solving Poisson's equation,

$$\nabla.\mathbf{E}_\mathrm{s} = -4\pi e n_\mathrm{b}(r), \tag{17}$$

where $-e$ is the electron charge. Solving (17) for $r \le r_\mathrm{b}$ and is zero otherwise, we obtain

$$\mathbf{E}_\mathrm{s} = -2\pi e n_\mathrm{b}\left(x\hat{e}_x + y\hat{e}_y\right). \tag{18}$$

The lowest-order representation for the self-magnetic field is obtained under the assumption that the beam propagates paraxially with $\mathbf{v} = v_\parallel\hat{e}_z$ in the interior of the beam. In this case, the self-magnetic field is determined by Ampere's law,

$$\nabla \times \mathbf{B}_\mathrm{s} = (4\pi/c)\,\mathbf{J}, \tag{19}$$

where c is the speed of light in a vacuum, $\mathbf{J}$ ($= -en_\mathrm{b}c\boldsymbol{\beta}_\parallel\hat{e}_z$) is the electron current density, and $\boldsymbol{\beta}_\parallel$ ($= \mathbf{v}_\parallel/c$) is the normalized electron axial velocity. The solution of equation (19), known as the axial velocity-induced self-magnetic field, may be expressed in the form

$$\mathbf{B}_\mathrm{s} = \mathbf{B}_{\mathrm{s}\parallel} = 2\pi e n_\mathrm{b}\beta_\parallel\left(y\hat{e}_x - x\hat{e}_y\right). \tag{20}$$

Single electron motion with rest mass m in these combined fields can be determined by the solution of the relativistic Lorentz equation,

$$\frac{\mathrm{d}(m\gamma\mathbf{v})}{\mathrm{d}t} = -e\left[\mathbf{E} + \frac{1}{c}(\mathbf{v}\times\mathbf{B})\right]. \tag{21}$$

With the aid of field equations (15), (16), (18) and (20), the steady-state (γ = constant) solution of equation (21) for the normalized wiggler-induced electron velocity in this configuration leads to

$$\boldsymbol{\beta}_\mathrm{w}^0 = \beta_{\mathrm{w}x}^0 \cos(k_\mathrm{l}z + \omega_\mathrm{l}t)\hat{e}_x + \beta_{\mathrm{w}y}^0 \sin(k_\mathrm{l}z + \omega_\mathrm{l}t)\hat{e}_y, \tag{22}$$

where

$$\beta_{\mathrm{w}x}^0 = \frac{\Omega_\mathrm{l}\left(\beta_\parallel + \beta_\mathrm{p}\right)^2\left[\left(\beta_\parallel + \beta_\mathrm{p}\right)^2 + \omega_\mathrm{b}^2\left(1 - \beta_\parallel^2\right)\right]}{\Omega_0^2\left(\beta_\parallel + \beta_\mathrm{p}\right)^2 - \left[\left(\beta_\parallel + \beta_\mathrm{p}\right)^2 + \omega_\mathrm{b}^2\left(1 - \beta_\parallel^2\right)\right]^2}, \tag{23}$$

$$\beta_{\mathrm{w}y}^0 = \frac{\Omega_0\Omega_\mathrm{l}\left(\beta_\parallel + \beta_\mathrm{p}\right)^3}{\Omega_0^2\left(\beta_\parallel + \beta_\mathrm{p}\right)^2 - \left[\left(\beta_\parallel + \beta_\mathrm{p}\right)^2 + \omega_\mathrm{b}^2\left(1 - \beta_\parallel^2\right)\right]^2}, \tag{24}$$

β_p ($\equiv \omega_\mathrm{l}/ck_\mathrm{l}$) denotes the normalized phase velocity for the laser wiggler, ω_b [$\equiv (2\pi e^2 n_\mathrm{b}/m\gamma k_\mathrm{l}^2c^2)^{1/2}$] denotes the normalized beam frequency, and $\Omega_{0,\mathrm{l}}$ ($\equiv eB_{0,\mathrm{l}}/m\gamma k_\mathrm{l}c^2$) are normalized axial guide and laser-wiggler magnetic fields, respectively.

The transverse electron velocity induced by the wiggler magnetic field generates another self-magnetic field known as a wiggler-induced self-magnetic field and we denote it as $\mathbf{B}_\mathrm{sw}$. Using Ampere's law [equation (19)], and following the procedure of Freund *et al.* (1993), results in the wiggler-induced self-magnetic field being proportional to the wiggler magnetic field as follows,

$$\mathbf{B}_\mathrm{sw}^1 = \lambda_x^1 B_\mathrm{l}\cos(k_\mathrm{l}z + \omega_\mathrm{l}t)\hat{e}_x + \lambda_y^1 B_\mathrm{l}\sin(k_\mathrm{l}z + \omega_\mathrm{l}t)\hat{e}_y. \tag{25}$$

The first-order wiggler-induced self-magnetic field [equation (25)] also causes a new transverse velocity. Resolving the equation of motion [equation (21)], the normalized electron transverse velocity components can be written as

$$\beta_{\mathrm{w}x}^1 = \left[\lambda_x^1\beta_{\mathrm{w}y}^0 + (1 + \lambda_y^1)\beta_{\mathrm{w}x}^0\right]\cos(k_\mathrm{l}z + \omega_\mathrm{l}t), \tag{26}$$

$$\beta_{\mathrm{w}y}^1 = \left[\lambda_x^1\beta_{\mathrm{w}x}^0 + (1 + \lambda_y^1)\beta_{\mathrm{w}y}^0\right]\sin(k_\mathrm{l}z + \omega_\mathrm{l}t). \tag{27}$$

Consequently, the above transverse velocity produces a new wiggler-induced self-magnetic field

$$\mathbf{B}_\mathrm{sw}^2 = \lambda_x^2 B_\mathrm{l}\cos(k_\mathrm{l}z + \omega_\mathrm{l}t)\hat{e}_x + \lambda_y^2 B_\mathrm{l}\sin(k_\mathrm{l}z + \omega_\mathrm{l}t)\hat{e}_y, \tag{28}$$

and so on. This process may be continued to find the higher-order terms. Using Ampere's law,

$$\nabla \times \mathbf{B}_\mathrm{sw}^{n+1} = -4\pi e n_\mathrm{b}\boldsymbol{\beta}^n, \tag{29}$$

we can obtain

$$\lambda_x^{n+1} = A_1\lambda_x^n + A_2\left(1 + \lambda_y^n\right), \tag{30}$$

$$\lambda_y^{n+1} = A_2\lambda_x^n + A_1\left(1 + \lambda_y^n\right), \tag{31}$$

where $n \ge 1$,

$$A_1 \equiv \frac{2\omega_\mathrm{b}^2\left(\beta_\parallel + \beta_\mathrm{p}\right)^2\left[\left(\beta_\parallel + \beta_\mathrm{p}\right)^2 + \omega_\mathrm{b}^2\gamma_\parallel^{-2}\right]}{\Omega_0^2\left(\beta_\parallel + \beta_\mathrm{p}\right)^2 - \left[\left(\beta_\parallel + \beta_\mathrm{p}\right)^2 + \omega_\mathrm{b}^2\gamma_\parallel^{-2}\right]^2}, \tag{32}$$

$$A_2 \equiv \frac{2\omega_b^2\Omega_0(\beta_\parallel+\beta_p)^3}{\Omega_0^2(\beta_\parallel+\beta_p)^2-\left[(\beta_\parallel+\beta_p)^2+\omega_b^2\gamma_\parallel^{-2}\right]^2}, \quad (33)$$

and $\gamma_\parallel = (1-\beta_\parallel^2)^{-1/2}$. Equations (30) and (31) may be rewritten in the form

$$D\lambda_x^{n+1} = F(1+D\lambda_x^n), \quad (34)$$

$$\lambda_y^{n+1} = F(1+\lambda_y^n), \quad (35)$$

where

$$D \equiv \frac{A_1(1-A_1)+A_2^2}{A_2}, \quad (36)$$

$$F \equiv \frac{A_1(1-A_1)+A_2^2}{(1-A_1)}. \quad (37)$$

Using equations (34) and (35), we can write

$$\lambda_x \equiv \lim_{n\to\infty}\lambda_x^n = \frac{1}{D}\left(F\sum_{i=0}^{\infty}F^i\right) = \frac{2\omega_b^2\Omega_0(\beta_\parallel+\beta_p)^3}{\Omega_0^2(\beta_\parallel+\beta_p)^2-\left[(\beta_\parallel+\beta_p)^2(1+2\omega_b^2)+\omega_b^2\gamma_\parallel^{-2}\right]^2}, \quad (38)$$

$$\lambda_y \equiv \lim_{n\to\infty}\lambda_y^n = F\sum_{i=0}^{\infty}F^i = \frac{2\omega_b^2(\beta_\parallel+\beta_p)^2\left[(\beta_\parallel+\beta_p)^2(1+2\omega_b^2)+\omega_b^2\gamma_\parallel^{-2}\right]}{\Omega_0^2(\beta_\parallel+\beta_p)^2-\left[(\beta_\parallel+\beta_p)^2(1+2\omega_b^2)+\omega_b^2\gamma_\parallel^{-2}\right]^2}, \quad (39)$$

The convergence condition for equations (38) and (39) is $|F| < 1$, which is in fact a restriction for the validity of this method for high e-beam density. Finally, the total wiggler-induced magnetic field becomes

$$\mathbf{B}_{sw} = B_{sw\perp}\cos(k_1 z+\omega_1 t)\hat{e}_x + B_{sw\parallel}\sin(k_1 z+\omega_1 t)\hat{e}_y, \quad (40)$$

where $B_{sw\perp} \equiv \lambda_x B_1$ and $B_{sw\parallel} \equiv \lambda_y B_1$.

The first component in equation (40) is perpendicular to the wiggler magnetic field B_w [equation (16)], while the second one is parallel ($\lambda_y > 0$) or antiparallel ($\lambda_y < 0$) to the wiggler magnetic field. The existence of the perpendicular component of the wiggler-induced self-magnetic field in a linearly polarized wiggler is the main discrepancy with the case of a circular polarized wiggler in which no perpendicular component exists. Because of providing the best analysis of the self-field effects on the FEL gain, numerical results of the wiggler-induced self-magnetic field are presented at the end of §5 in Fig. 15.

Now we can study electron dynamics in a FEL with linearly polarized laser wiggler and axial magnetic field in the presence of the self-fields. Substituting equations (15), (16), (18), (20) and (40) into (21), the scalar steady-state (γ = constant) equations of motion may be written in the form

$$\frac{d\beta_x}{d\tau} = \omega_b^2(1-\beta_\parallel\beta_z)X + (1+\lambda_y)(\beta_z+\beta_p)\Omega_1\sin(Z+\beta_p\tau) - \Omega_0\beta_y, \quad (41)$$

$$\frac{d\beta_y}{d\tau} = \omega_b^2(1-\beta_\parallel\beta_z)Y - \lambda_x(\beta_z+\beta_p)\Omega_1\cos(Z+\beta_p\tau) + \Omega_0\beta_x, \quad (42)$$

$$\frac{d\beta_z}{d\tau} = \omega_b^2\beta_\parallel(X\beta_x+Y\beta_y) - \Omega_1\left[\lambda_x\beta_y\cos(Z+\beta_p\tau) - (1+\lambda_y)\beta_x\sin(Z+\beta_p\tau)\right], \quad (43)$$

where $X = xk_w$, $Y = yk_w$, $Z = zk_w$ are normalized coordinates and $\tau = tck_w$ is the normalized time.

Electrons, moving in the wiggler magnetic field, are deviated from straight trajectories by the Lorentz force perpendicular to their direction. The electrons enter circular orbits of radius r_c, which is called the Larmor or cyclotron radius of an electron. An electron will be deviated by the electric component E_1 of the laser wiggler and will start to move in the negative x direction following turning the laser on. However, from this moment, the bending effects of the magnetic component B_1 of the laser wiggler and the static guide magnetic field B_0 will start to influence the electron. The component B_1 will tend to bend the electron trajectory around the y axis while the component B_0 will tend to make the electron follows a helix around the z axis. The result of these combined actions is a helical trajectory with superimposed wiggles.

Using the fourth-order Runge–Kutta method with adaptive step size for coupled differential dynamic equations (41)–(43), a graph of the normalized transverse displacements of the electron *versus* the normalized interaction time in a FEL region for various axial guide magnetic field strengths Ω_0 is shown in Fig. 5. The normalized coordinates X and Y are significantly smaller than the Z coordinate and this difference is more pronounced at larger Ω_0. Hence, the dimensions of the trajectories in the (X, Y) plane are subject to variation depending on the value of Ω_0. A cross-section view of electron motion in the case of various axial guide magnetic field strengths is plotted in Fig. 6. As can be seen, variation in Ω_0 results in variation not only in the trajectory size but also in its shape. In smaller amounts of Ω_0, the electron trajectory is not the shape of a perfect helix. As the normalized magnetic field frequency Ω_0 increases, the shape of the electron trajectory significantly changes. At high Ω_0, the electron is launched along a perfect helical path. Besides, this figure shows that the wiggle number of electrons increases with increasing axial guide magnetic field strength. In other words, this oscillation shows an increasing frequency (cyclotron frequency ω_c) with Ω_0 rising. Furthermore, in Fig. 7, a cross-section view of the electron motion in the case of various normalized beam frequencies ω_b is plotted. As is evident from this figure, in the absence of the self-field ($\omega_b = 0$) the electron is launched along a perfect helical path; as the normalized beam frequency ω_b increases, the shape of the electron trajectory becomes less helical.

After the numerical solutions to simulate the electron trajectories, we derive proper analytical solutions using appropriate assumptions. The importance of the analytic

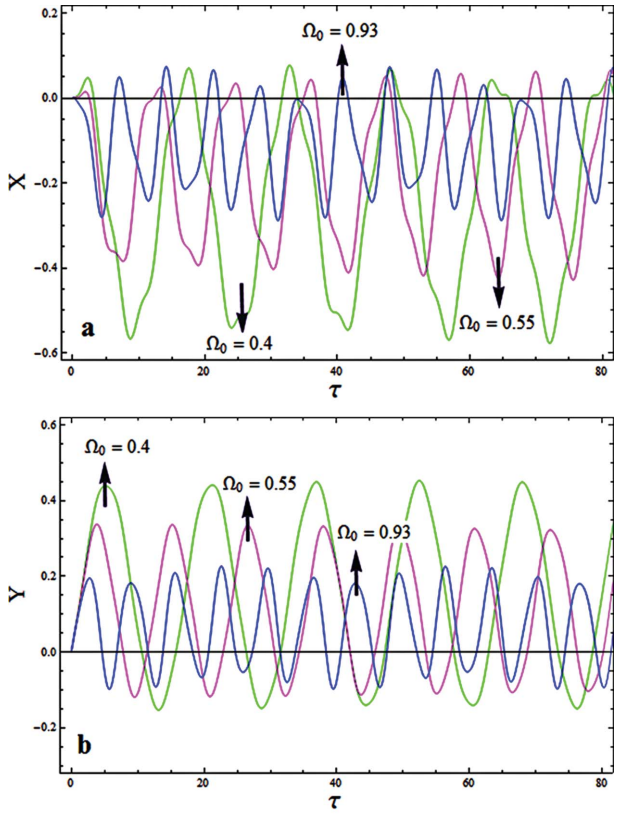

Figure 5
Graph of the normalized transverse components of the electron trajectory *versus* the normalized interaction time for (*a*) (τ, X) and (*b*) (τ, Y) when $\gamma = 25$, $\Omega_l = 0.05$, $\omega_b = 0.1$, $\Omega_0 = 0.4$, 0.55 and 0.93.

solution lies in the fact that it leads to a deeper insight into the problem in hand, and hence to a better understanding of the physics involved. The analytical solutions of equations (41)–(43) for the normalized transverse electron velocity components in the presence of all relevant fields, including wiggler, self-fields and axial guide magnetic fields, can be obtained as

$$\boldsymbol{\beta}_w = \beta_{wx}\cos(k_l z + \omega_l t)\hat{\boldsymbol{e}}_x + \beta_{wy}\sin(k_l z + \omega_l t)\hat{\boldsymbol{e}}_y, \qquad (44)$$

where

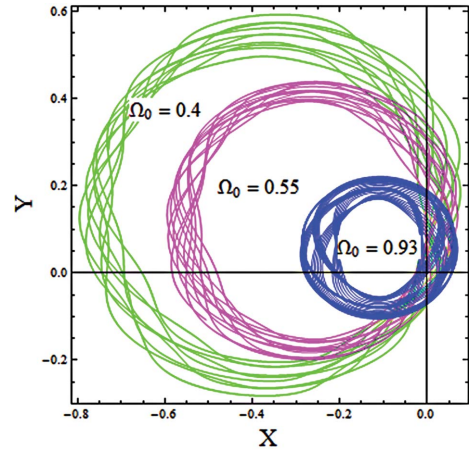

Figure 6
Cross-section view of the electron motion for $\gamma = 25$, $\Omega_l = 0.05$, $\omega_b = 0.1$, $\Omega_0 = 0.4$, 0.55 and 0.93.

$$\beta_{wx} = \frac{\Omega_l(\beta_\parallel + \beta_p)^2\left[(\beta_\parallel + \beta_p)^2(1+2\omega_b^2) + \omega_b^2\gamma_\parallel^{-2}\right]}{\Omega_0^2(\beta_\parallel + \beta_p)^2 - \left[(\beta_\parallel + \beta_p)^2(1+2\omega_b^2) + \omega_b^2\gamma_\parallel^{-2}\right]^2}, \qquad (45)$$

$$\beta_{wy} = \frac{\Omega_l\Omega_0(\beta_\parallel + \beta_p)^3}{\Omega_0^2(\beta_\parallel + \beta_p)^2 - \left[(\beta_\parallel + \beta_p)^2(1+2\omega_b^2) + \omega_b^2\gamma_\parallel^{-2}\right]^2}. \qquad (46)$$

In the limit $\omega_b = 0$, equations (35) and (36) reduce to the well known wiggler-induced transverse velocities in the absence of self-fields. These equations also show a resonant enhancement. Setting the denominator equal to zero gives the characterization of two classes of trajectories called group I and group II orbits, defined by

$$\Omega_0 < \frac{1}{(\beta_\parallel + \beta_p)}\left[(\beta_\parallel + \beta_p)^2(1+2\omega_b^2) + \omega_b^2\gamma_\parallel^{-2}\right] \qquad (47)$$

and

$$\Omega_0 > \frac{1}{(\beta_\parallel + \beta_p)}\left[(\beta_\parallel + \beta_p)^2(1+2\omega_b^2) + \omega_b^2\gamma_\parallel^{-2}\right], \qquad (48)$$

respectively.

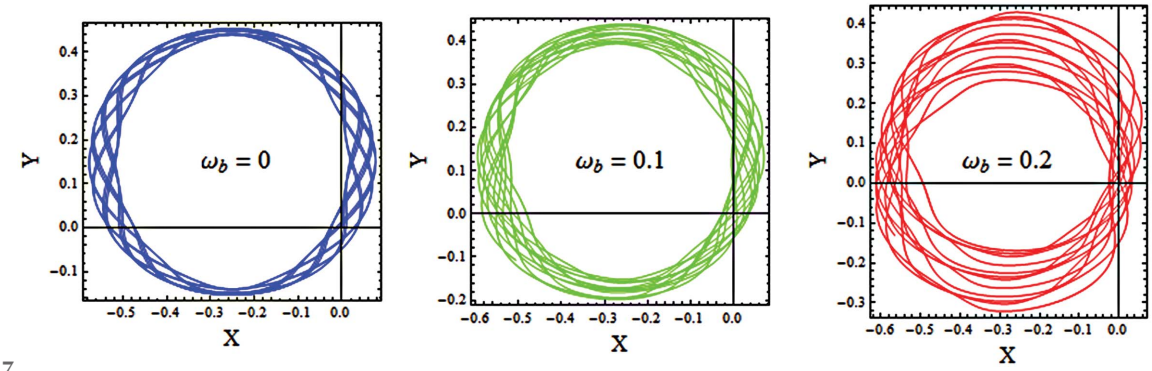

Figure 7
Cross-section view of the electron motion for $\gamma = 25$, $\Omega_l = 0.05$, $\Omega_0 = 0.4$, $\omega_b = 0$, 0.1 and 0.2.

As can be seen from the simulation presented in graphical form using the Runge–Kutta method, equilibrium orbits at some specially selected values of the axial guide magnetic field are axis-centered helices with a constant radius. In other words, the projections of the trajectories onto the (X, Y) plane do not change in time in spite of proceeding circulations, which means that their shapes in each cycle appear to be the same. Therefore, the energy of the electrons represented by the relativistic factor γ is constant because the distance from the axis remains the same for each trajectory. We call these trajectories or their projections the stationary ones. However, the energy of the electron is a constant of motion only when averaged over cycles. On the other hand, equilibrium trajectories in the presence of the weak axial guide magnetic field are not axis centered, and γ is approximately constant. For these near steady-state orbits, however, γ is not exactly constant and in the stability analysis of equilibrium orbits the distance from the axis varies for both on- and off-axis orbits and a small change in γ can make a stable trajectory unstable and *vice versa*. The stability analysis, under the constant γ approximation, is presented in Appendix *A*. It shows that the self-fields can make parts of the steady-state orbits unstable. These instability regions will be widened to cover the entire group I and group II orbits if the defocusing effects of the self-fields are increased sufficiently.

The frequency and wavenumber of a laser wiggler are not independent parameters, but they are specified by the dielectric properties of the medium. The dispersion equation is obtained by substitution of the electron current into Maxwell's equations, and the result is

$$\beta_p{}^2 - 1 + \frac{2\omega_b^2\left(\beta_\parallel+\beta_p\right)^2\left[\left(\beta_\parallel+\beta_p\right)^2\left(1+2\omega_b^2\right)+\omega_b^2\gamma_\parallel^{-2}\right]}{\Omega_0^2\left(\beta_\parallel+\beta_p\right)^2-\left[\left(\beta_\parallel+\beta_p\right)^2\left(1+2\omega_b^2\right)+\omega_b^2\gamma_\parallel^{-2}\right]^2}=0. \tag{49}$$

For fixed values of γ, Ω_l and ω_b, equations (44), (49) and $1-\beta_w^2-\beta_\parallel^2-\gamma^{-2}=0$ are sufficient to determine the normalized e-beam axial velocity $\beta_\parallel$ and normalized phase velocity β_p. A plot of $\beta_\parallel$ of group I orbits (*a*) and group II orbits (*b*) against the axial guide magnetic field frequency Ω_0 for chosen acceptable values is shown in Fig. 8. In addition, a plot of $\beta_\parallel$ for both the planar magnetostatic wiggler and the linearly polarized laser wiggler is shown in Fig. 9 (we investigate the planar wiggler for comparison). A plot of β_p against Ω_0 is shown in Fig. 10.

4. Gain equation of the laser wiggler

The present analysis assumes a relativistic electron beam accompanied by its electromagnetic radiation propagating in the FEL interaction region. The electric and magnetic field of radiation may be written as

$$\mathbf{E}_r = E_r(\cos\xi\hat{e}_x - \sin\xi\hat{e}_y), \tag{50}$$

$$\mathbf{B}_r = E_r(\sin\xi\hat{e}_x + \cos\xi\hat{e}_y), \tag{51}$$

where $\xi \equiv k_r z - \omega_r t + \varphi$, k_r is the wavenumber, ω_r is the angular frequency of the radiation wave, and φ is a phase constant. Assuming β_z is close to 1, the normalized component of the electron velocity in the presence of self-fields and electromagnetic radiation has been found to be the same as that found previously in §3 by the self-consistent method [equation (44)]. The transverse motion is directly coupled to the longitudinal motion because the energy is constant. So the average of the normalized axial velocity over a wiggler period, β_z can be expanded, for $\gamma \gg 1$, as

$$\beta_z \cong 1 - \frac{1}{2}\gamma^{-2}\left[1+\frac{a_l^2\left(\beta_\parallel+\beta_p\right)^4\left(\theta^2+\delta^2\right)}{2\left(\theta^2-\delta^2\right)^2}\right], \tag{52}$$

where $a_l \equiv \gamma\Omega_l$, $\delta \equiv \left(1+2\omega_b^2\right)\left(\beta_\parallel+\beta_p\right)^2+\omega_b^2\gamma_\parallel^{-2}$ and $\theta \equiv \Omega_0\left(\beta_\parallel+\beta_p\right)$.

The energy exchange of the electron with the radiation field is given by

$$\dot{\gamma} = -\frac{e}{mc}\,\boldsymbol{\beta}\,.\,\mathbf{E}_r. \tag{53}$$

Substituting equations (44) and (50) into (53) yields

$$\dot{\gamma} = -\frac{eE_r}{2mc}\Big[\left(\beta_{wx}+\beta_{wy}\right)\cos(\Omega t+\varphi) + \left(\beta_{wx}-\beta_{wy}\right)\cos(\Omega' t+\varphi)\Big], \tag{54}$$

where $\Omega \equiv (k_r+k_l)c\beta_\parallel + (\omega_l-\omega_r)$ and $\Omega' \equiv (k_r-k_l)c\beta_\parallel-(\omega_l+\omega_r)$. Due to the rotating wave approximation for eliminating rapid oscillations, the second term in (54) can be neglected. Averaging this equation over all phases to first order yields no net energy exchange between the electron beam and the radiated wave. Therefore, the second-order correction can be achieved as

$$\dot{\gamma} = -\frac{eE_r}{2mc}\left(\beta_{wx}+\beta_{wy}\right)\cos\Big\{\Omega t+\varphi + D\big[\cos(\Omega t+\varphi)-\cos\varphi+\Omega t\sin\varphi\big]\Big\}, \tag{55}$$

where $D \equiv k^2(k_r+k_l)/\Omega^2$. Consequently, the lowest-order non-zero rate of change in energy averaged over the initial phase of radiation, φ, becomes

$$\langle\dot{\gamma}\rangle_\varphi = \frac{eE_rD(\beta_{wy}+\beta_{wy})}{4mc}\,(\Omega t\cos\Omega t-\sin\Omega t). \tag{56}$$

Integrating (56) over the electron transit time through the wiggler interaction length L yields the average change in γ per electron,

$$\langle\Delta\gamma\rangle_\varphi = \int_0^{T=L/c\beta_\parallel}\langle\dot{\gamma}\rangle_\varphi\,\mathrm{d}t = -\frac{eE_rD\Omega^2T^3\left(\beta_{wy}+\beta_{wy}\right)}{4mc}g(\Omega T). \tag{57}$$

Here,

$$g(\Omega T) = \frac{1}{(\Omega T)^3}(2-2\cos\Omega T-\Omega T\sin\Omega T) \tag{58}$$

denotes the gain function, which is defined as the relative energy increase of the light wave during one passage of the wiggler. The extremes of the gain occur at $\Omega T = \pm 2.6$ yielding $g(\Omega T) \cong \pm 0.135$, which corresponds to the wavenumbers

$$k_r = \frac{k_1}{(1-\beta_\parallel)}\left[(\beta_\parallel + \beta_p) \mp 2.6\frac{\beta_\parallel}{k_1 L}\right]. \quad (59)$$

The change in electromagnetic power in one transit is

$$\Delta P_r = -mc^3\beta_\parallel n_b \pi r_b^2 \langle \Delta\gamma\rangle_\varphi. \quad (60)$$

Finally, by using (57), (59) and (60) the linear gain can be written as

$$G_{max} \equiv \frac{\Delta P_r}{P_r} = \pm 0.07\frac{\pi k_1 e^2 n_b L^3 (1+\beta_\parallel)(\beta_{wx}+\beta_{wy})^2}{mC^2\beta_\parallel^2\gamma} \times F\left(1+\beta_p \mp 2.6\frac{\beta_\parallel}{k_1 L}\right), \quad (61)$$

where $P_r \equiv (E_r^2/4\pi)c\pi r_b^2$ is the electromagnetic power and

$$F \equiv \frac{1}{\gamma_\parallel^2}\left[1 - \frac{a_1^2(\beta_\parallel+\beta_p)^4\left\{\theta^4 - \delta^4 + (\beta_\parallel+\beta_p)^2\delta(3\theta^2+\delta^2)\right\}}{2(\theta^2-\delta^2)^3 + a_1^2(\beta_\parallel+\beta_p)^4(\theta^4-\delta^4)}\right]. \quad (62)$$

The $\pm$ signs must be chosen to give a positive gain in equation (61). In the limit $\omega_b \to 0$ (eliminating self-fields), the maximum gain reduces to

$$G_{max\,0} = \pm 0.07\frac{\pi k_1 e^2 n_b L^3(1+\beta_\parallel)}{mC^2\beta_\parallel^2\gamma}\left(1+\beta_p \mp 2.6\frac{\beta_\parallel}{k_1 L}\right) \times \left[\frac{\Omega_1(\beta_\parallel+\beta_p)}{\Omega_0 - (\beta_\parallel+\beta_p)}\right]^2 F_0, \quad (63)$$

where

$$F_0 = 1 - \Omega_0^2 a_1^2(\beta_\parallel+\beta_p)^2 \times \left\{\frac{\Omega_0^2 + 3(\beta_\parallel+\beta_p)^2}{2\left[\Omega_0^2 - (\beta_\parallel+\beta_p)^2\right]^3 + a_1^2(\beta_\parallel+\beta_p)^2\left[\Omega_0^4 - (\beta_\parallel+\beta_p)^4\right]}\right\}. \quad (64)$$

Similarly, if we set the normalized axial magnetic field, Ω_0, equal to zero in equation (63), we obtain

$$G_0 = \pm 0.07\frac{\pi k_1 e^2 n_b L^3(1+\beta_0)}{mC^2\beta_0^2\gamma}\Omega_1^2\left(1+\beta_p \mp 2.6\frac{\beta_0}{k_1 L}\right), \quad (65)$$

which is the maximum gain for a laser wiggler without guiding device and self-fields. Here, $\beta_0 = (1-\Omega_1^2-\gamma^{-2})^{1/2}$ is the normalized axial velocity in such a wiggler. Besides, if we set $\beta_p \to 0$, the above gain equations reduce to the gain equations for a planar magnetostatic wiggler.

5. Numerical studies and discussions

A numerical study of the self-field effects on the electron orbits and gain in a linearly polarized laser-wiggler FEL with axial guiding magnetic field has been made. The following values of the parameters have been chosen: the normalized laser magnetic field Ω_1 was taken to be 0.05; the e-beam energy $(\gamma-1)mc^2$ was taken to be 12.2 MeV, which corresponds to a Lorentz factor γ of 25; and the normalized e-beam frequency ω_b was taken to be 0.1.

A graph of the normalized e-beam axial velocity, $\beta_\parallel$, as a function of the normalized axial guide magnetic field frequency, Ω_0, for the laser wiggler in the presence of the self-fields has been shown in Fig. 8. Here, the electron trajectories are divided into two groups; Group I (Fig. 8*a*) and group II (Fig. 8*b*) orbits are defined by the conditions of equations (47) and (48), respectively. The results in the absence of self-fields are shown for comparison, by dotted lines. Numerical calculation (Appendix *A*) shows that the upper branches (continuous line) for group I orbits both in the presence and absence of the self-fields are stable and the dashed lines are unstable. On the other hand, the orbits of group II are stable for all values of Ω_0, and in this group $\beta_\parallel$ increases with increasing axial guide magnetic field frequency. Numerical calculations also show that unstable orbits (of group I) in general depend on an e-beam frequency, ω_b, and decrease with increasing e-beam frequency until all orbits become stable. A comparison between the electron orbits with and without considering the self-fields indicates that the electron orbits for both groups approach each other. Moreover, in the presence of the self-

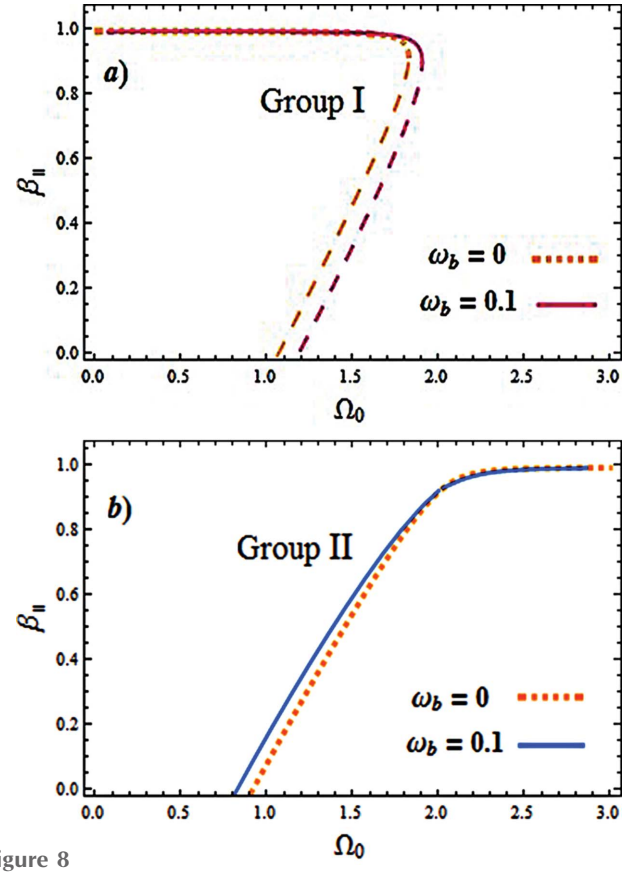

Figure 8
Graph of normalized axial velocity of (*a*) group I orbits and (*b*) group II orbits *versus* the normalized guide magnetic field frequency for $\omega_b = 0.1$, $\Omega_1 = 0.05$ and $\gamma = 25$. The dashed lines indicate the unstable orbits.

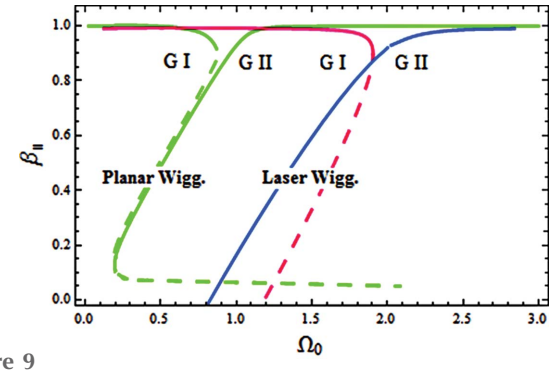

Figure 9
Graph of normalized axial velocity of group I orbits and group II orbits *versus* the normalized guide magnetic field frequency for the planar magnetostatic wiggler and linearly polarized laser wiggler. The chosen parameters are $\omega_b = 0.1$, $\Omega_l = 0.05$ and $\gamma = 25$. The dashed lines indicate the unstable orbits.

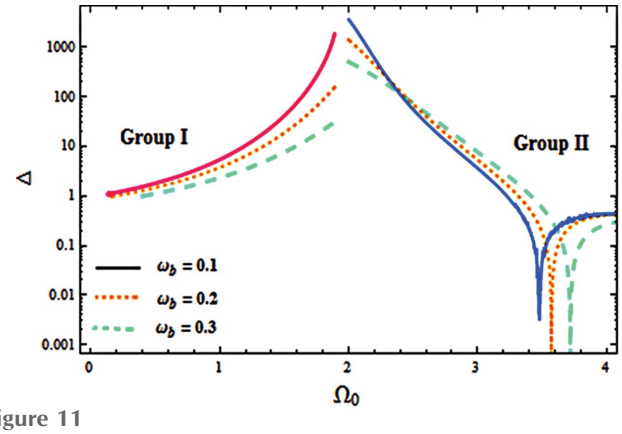

Figure 11
Graph of the normalized gain, Δ, *versus* the normalized guide magnetic field frequency for $\gamma = 25$, $\Omega_l = 0.05$, $\omega_b = 0.1$, 0.2 and 0.3.

fields, group II orbits are a multi-valued function of the normalized axial magnetic field frequency Ω_0, whereas, in the absence of self-fields, group II orbits are single-valued.

Besides, the graph of the normalized e-beam axial velocity as a function of Ω_0 for both the linearly polarized laser wiggler and the planar magnetostatic wiggler has been shown in Fig. 9 (we investigate the planar wiggler case for comparison). The main differences between electron orbits in these two types of wigglers are: (i) the resonance frequency of the orbits in the planar magnetostatic wiggler occurs around $\Omega_0 \approx 0.9$, while for the laser wiggler it occurs around $\Omega_0 \approx 1.9$, *i.e.* the resonant frequency (of the transverse velocity) of the laser wiggler is greater than the resonant frequency of the planar wiggler, and (ii) in the planar wiggler group II orbits exhibit an orbital instability which is not found in the laser wiggler.

Fig. 10 shows the dispersion relation of the laser wiggler [equation (49)]. As shown in this figure, there are two relevant modes for backward-propagating electromagnetic radiation, positive β_p: an electromagnetic escape mode and an electromagnetic electron cyclotron wave supported by the beam. Group I and II orbits correspond to waves in the electromagnetic escape mode and the electromagnetic electron cyclotron mode, respectively. Since $\omega_l > ck_l$, it is seen that the wiggler electromagnetic waves are supraluminous for group I orbits, while for the group II orbits, because $\omega_l < ck_l$, the wiggler waves are subluminous. Dashed lines indicate the unstable branch of group I orbits.

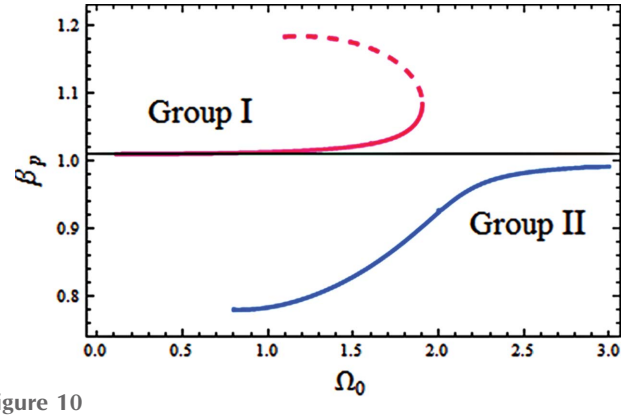

Figure 10
Graph of the dispersion relation as a function of the normalized axial guide magnetic field frequency for group I and II orbits. The chosen parameters are $\omega_b = 0.1$, $\Omega_l = 0.05$ and $\gamma = 25$. The dashed lines indicate the unstable orbits.

A graph of normalized gain, $\Delta \equiv G_{max}/G_0$ (*i.e.* the ratio of the maximum gain in the presence of the self-fields to maximum gain in the absence of the self-fields and axial guide magnetic field), as a function of the normalized axial magnetic field frequency for stable group I and group II orbits, is depicted in Fig. 11 (solid lines). It is shown that the normalized gain for group I orbits increases monotonically from 1 for $\Omega_0 = 0$ and reaches its peak (1943.46) at $\Omega_0 = 1.88$ near its transverse velocity resonance frequency (see the electron orbits in Fig. 8). For group II orbits, the normalized gain starts from $\Omega_0 \approx 1.97$, $\Delta \approx 3821.03$, which is near the resonant frequency, then goes down to zero at $\Omega_0 \equiv \Omega_0^{cr} = 3.48$, then goes up again until it reaches the maximum value of around 0.4. The zero gain in group II is due to the $F = 0$ in equation (61) in which the zero mass regime occurs. Note that, for group II orbits, F is less than zero for $\Omega_0 < \Omega_0^{cr}$ (negative mass regime) and F becomes greater than zero for $\Omega_0 > \Omega_0^{cr}$ (positive mass regime). In addition, it is worthwhile investigating the normalized gain, Δ, *versus* the different normalized beam frequencies, ω_b. It appears that the peak of the normalized gain for the group I orbits decreases with increasing normalized beam frequency, while for the group II orbits in $\Omega_0 = \Omega_0^{cr}$ the normalized gain starts going up to a maximum which increases with increasing normalized beam frequency.

A graph of the normalized gain, $\Delta \equiv G_{max}/G_0$, as a function of the normalized axial magnetic field frequency, is shown in Fig. 12 for both the planar magnetostatic wiggler and the linearly polarized laser wiggler for comparison. It appears that the normalized gain for a planar wiggler (dotted lines) is similar to the normalized gain for a laser wiggler (solid lines), but the normalized gain in the planar wiggler increases quite strongly to its peak (1009.36) for group I orbits, which is about half of the pick of the laser wiggler. The behavior of the normalized gain of group II orbits for the planar wiggler is similar to that of the laser, with a pick value of 1723.16 near its

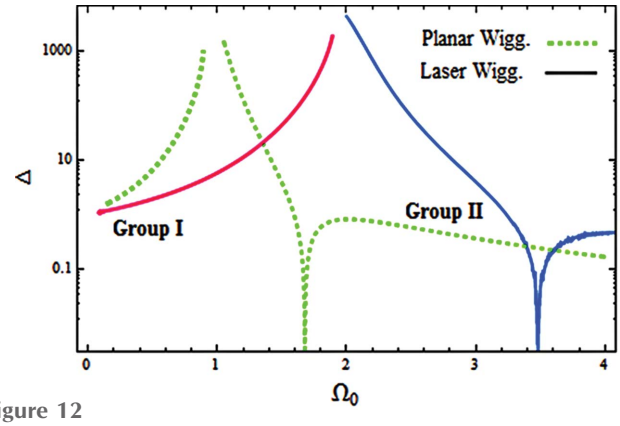

Figure 12
Graph of the normalized gain, Δ, for both linearly polarized laser (solid lines) and magnetostatic (dotted lines) wigglers *versus* the normalized axial guide magnetic field frequency. The chosen parameters are $\omega_b = 0.1$, $\Omega_l = 0.05$ and $\gamma = 25$.

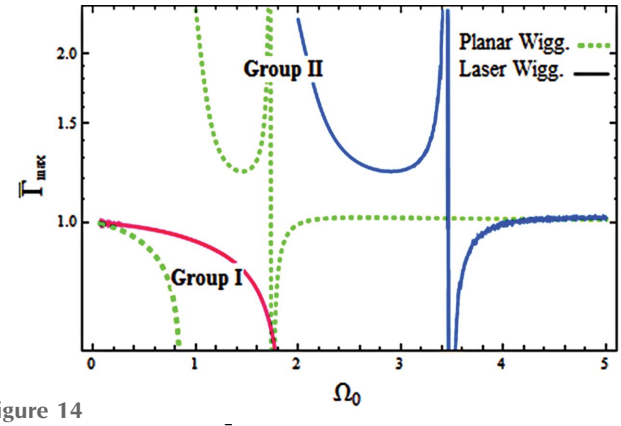

Figure 14
Graph of the gain ratio, $\bar{\Gamma}_{max}$, for both linearly polarized laser wiggler (solid lines) and planar magnetostatic wiggler (dotted lines) *versus* the normalized axial guide magnetic field frequency. The chosen parameters are $\omega_b = 0.1$, $\Omega_l = 0.05$ and $\gamma = 25$.

resonant frequency, which is less than half of the laser pick (*i.e.* 3821.03). As a result, the resonant frequency and the normalized gain near the resonant frequency for the laser wiggler are much higher than for the planar wiggler.

The graph of the gain ratio, $\overline{\Gamma}_{max} \equiv G_{max}/G_{max\,0}$ (*i.e.* the ratio of the maximum gain in the presence of the self-fields to the maximum gain in the absence of the self-fields), for group I and II orbits as a function of the normalized axial magnetic field frequency, Ω_0 is illustrated in Fig. 13. As shown in the figure, for group I orbits the gain ratio is less than 1 and therefore a gain decrement is obtained due to the self-fields, and this decrement is more for stronger self-fields (or greater ω_b). This gain decrement, with increasing Ω_0, increases very slowly, while for group II orbits the gain ratio is greater than 1, except for the critical point, $\Omega_0 \equiv \Omega_0^{cr} = 3.48$ (solid lines). Therefore, the gain enhancement is obtained due to the self-fields, and it increases with increasing ω_b. It is seen that this gain enhancement starts from $\Omega_0 \approx 1.97$, $\overline{\Gamma}_{max} \approx 2.3$, then with increasing Ω_0 it decreases to its minimum near to the critical point and then increases. Note that the zero and singular points in this figure are due to the different zero point of maximum gain in the presence and absence of the self-fields, respectively, and are not physically important.

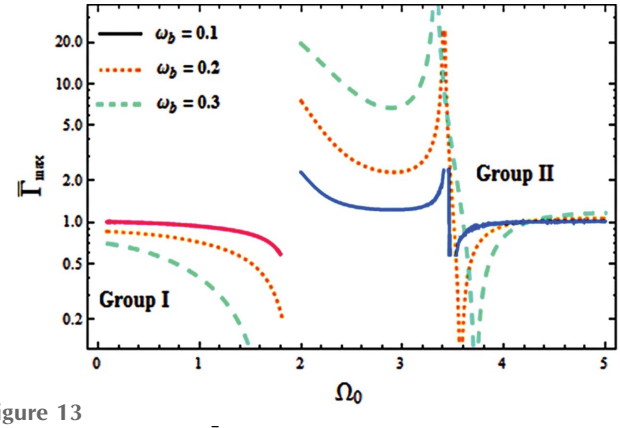

Figure 13
Graph of the gain ratio, $\bar{\Gamma}_{max}$, *versus* the normalized guide magnetic field frequency for $\gamma = 25$, $\Omega_l = 0.05$, $\omega_b = 0.1$, 0.2 and 0.3.

Furthermore, Fig. 14 shows the gain ratio, $\overline{\Gamma}_{max} \equiv G_{max}/G_{max\,0}$, as a function of the normalized axial magnetic field frequency, Ω_0, for both the planar magnetostatic wiggler (dotted lines) and the linearly polarized laser wiggler (solid lines). As seen in this figure, the gain for both planar wiggler and laser wiggler for group I orbits are less than 1, and the effect of self-fields cause the gain decrement, but this gain decrement for the planar wiggler is greater than that for the laser wiggler. On the other hand, for group II orbits, the gain ratio for both laser wiggler and planar wiggler are greater than 1 except near their critical points, therefore the gain enhancement is obtained due to the self-fields. The gain enhancement for the planar wiggler has an almost similar behavior to that of the laser wiggler, starting from $\Omega_0 \approx 0.9$, near its transverse velocity resonance frequency, and goes down to its minimum near to the critical point $\Omega_0 \equiv \Omega_0^{cr} = 1.73$ and then increases.

Graphs of the normalized parallel (or antiparallel) component of the wiggler-induced self-magnetic field $\bar{B}_{sw\parallel}$ ($\equiv B_{sw\parallel}/B_w$) as well as the normalized perpendicular component of the wiggler-induced self-magnetic field $\bar{B}_{sw\perp}$ ($\equiv B_{sw\perp}/B_w$) are shown in Fig. 15. As we see in this figure, $\bar{B}_{sw\parallel}$ is negative (antiparallel to the wiggler magnetic field) for group I orbits while it is positive (parallel to the wiggler magnetic field) for group II orbits. The perpendicular component of the normalized wiggler-induced self-magnetic field $\bar{B}_{sw\perp}$ (dashed lines) is also negative for group I orbits and positive for group II orbits. Therefore, the wiggler-induced self-magnetic field decreases the effective wiggler magnetic field and has a diamagnetic effect for group I orbits. For group II orbits it increases the effective wiggler magnetic field and has a paramagnetic effect. Although the graphs of the parallel (or antiparallel) and perpendicular components are similar, the absolute value of the antiparallel component is greater than that of the perpendicular component for group I orbits, whereas for group II orbits the perpendicular component is greater than the parallel one. Thus we conclude that for group I orbits the gain decrement relative to the absence of the self-fields is only due to the diamagnetic effects of the wiggler-

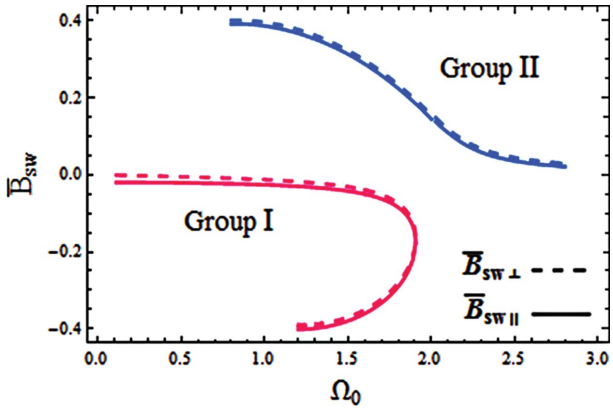

Figure 15
Graphs of the normalized parallel (or antiparallel) and perpendicular components of wiggler-induced self-magnetic fields (*i.e.* $B_{sw\parallel}$ and $B_{sw\perp}$) as a function of the normalized axial magnetic field frequency. The solid and dashed lines indicate $B_{sw\parallel}$ and $B_{sw\perp}$, respectively.

induced self-magnetic field, and the gain enhancement in group II orbits is due to the paramagnetic effects of the wiggler-induced self-magnetic field. It was also found from Figs. 11 and 13 that the diamagnetic (paramagnetic) effect for group I (group II) orbits increases with increasing normalized beam frequency (beam density). As a consequence, the beam density plays an important role in controlling both the resonance point and suitable frequency of the output radiations of the laser-wiggler FELs.

6. Conclusion

In this work, we investigated the working conditions of FELs operating with a laser-wave wiggler. We provided general scaling criteria and corroborated them with appropriate numerical simulations. The electron orbits and FEL gain in the presence of the combined effects of the laser-wiggler field, the self-fields and the external focusing magnetic field were derived. The wiggler-induced self-magnetic field associated with the charge density and current of the electron beam was derived by a self-consistent method. The electron trajectory schemes obtained by the fourth-order Runge–Kutta method showed that in the intense laser field and strong magnetic field the electron trajectory is a helix (with superimposed wiggles). However, external magnetic fields increase the results in shrinking of the trajectories. Equilibrium steady-state orbits showed that the self-fields modify the group I and group II orbits. A comparison between the electron orbits of a linearly polarized laser-wiggler and a planar magnetostatic wiggler was made and the results indicated that the resonant frequency of the laser wiggler is greater than the resonant frequency of the planar magnetostatic wiggler. Furthermore, in the planar wiggler, group II orbits exhibit an orbital instability which is not found in the laser wiggler. The self-fields play an important role in controlling both the resonance point and suitable frequency of the output radiations of the laser-wiggler FELs. Numerical results indicated a gain decrement for group I orbits and a gain enhancement for group II orbits, since the wiggler-induced self-magnetic field had a diamagnetic effect on group I orbits whereas for group II it had a paramagnetic effect. These diamagnetic and paramagnetic effects increased with increasing beam density. A comparison of the FEL gain for the linearly polarized laser wiggler with the FEL gain for the planar magnetostatic wiggler showed that the resonant frequency and the peak gain for the laser wiggler are much higher than that of the planar wiggler.

APPENDIX *A*
The stability of electron orbits in the laser wiggler

For analyzing the stability of orbits, we find it convenient to work in the reference frame rotating with the laser wiggler, and define the basis vectors

$$\hat{e}_1 = \hat{e}_x \cos(k_1 z + \omega_1 t) + \hat{e}_y \sin(k_1 z + \omega_1 t), \tag{66}$$

$$\hat{e}_2 = -\hat{e}_x \sin(k_1 z + \omega_1 t) + \hat{e}_y \cos(k_1 z + \omega_1 t), \tag{67}$$

$$\hat{e}_3 = \hat{e}_z. \tag{68}$$

The scalar equations of motion in this frame are

$$\frac{d\beta_1}{d\tau} = \omega_b^2(1-\beta_3^2)\chi_1 + \lambda_-(\beta_3+\beta_p)\Omega_1 \sin\eta - \left[\Omega_0 - (\beta_3+\beta_p)\right]\beta_2, \tag{69}$$

$$\frac{d\beta_2}{d\tau} = \omega_b^2(1-\beta_3^2)\chi_2 + (\beta_3+\beta_p)\Omega_1\left[\lambda_- \cos\eta - \lambda_+\right] + \left[\Omega_0 - (\beta_3+\beta_p)\right]\beta_1, \tag{70}$$

$$\frac{d\beta_3}{d\tau} = \omega_b^2\beta_3(\beta_1\chi_1 + \beta_2\chi_2) - \Omega_1\left[\beta_1\lambda_- \sin\eta + \beta_2(\lambda_- \cos\eta - \lambda_+)\right], \tag{71}$$

where $\chi \equiv k_1 x$ is the normalized electron position, $\eta \equiv 2(\chi_3 + \beta_p\tau)$ and $\lambda_\pm \equiv (1+\lambda_y \pm \lambda_x)/2$.

The steady-state solutions of equations (69)–(71) may be written as

$$\beta_{10} = \alpha_+ + \alpha_- \cos\eta, \tag{72}$$

$$\beta_{20} = -\alpha_- \sin\eta, \tag{73}$$

$$\beta_{30} = \beta_\parallel, \tag{74}$$

for the unperturbed (subscript zero) normalized electron velocity components and

$$\chi_{10} = \frac{\alpha_- \sin\eta}{(\beta_\parallel + \beta_p)}, \tag{75}$$

$$\chi_{20} = \frac{\alpha_- \cos\eta - \alpha_+}{(\beta_\parallel + \beta_p)}, \tag{76}$$

$$\chi_{30} = \beta_\parallel \tau, \tag{77}$$

for the unperturbed normalized position components, where

$$\alpha_{\pm} \equiv \frac{\Omega_1(\beta_\parallel+\beta_p)^2\left\{\left[(\beta_\parallel+\beta_p)^2(1+2\omega_b^2)+\omega_b^2\gamma_\parallel^{-2}\right]\pm\Omega_0(\beta_\parallel+\beta_p)\right\}}{\Omega_0^2(\beta_\parallel+\beta_p)^2-\left[(\beta_\parallel+\beta_p)^2(1+2\omega_b^2)+\omega_b^2\gamma_\parallel^{-2}\right]^2}. \quad (78)$$

The stability of the steady-state orbits can be determined as follows. The electron fluid variables will each be written as an unperturbed part plus a small perturbation, $\chi = \chi_0 + \delta\chi$, and $\beta = \beta_0 + \delta\beta$. The relations between the normalized transverse position coordinates in the wiggler frame and normalized velocity components are given by

$$\beta_1 = \frac{d\chi_1}{d\tau} - (\beta_3+\beta_p)\chi_2, \quad (79)$$

$$\beta_2 = \frac{d\chi_2}{d\tau} + (\beta_3+\beta_p)\chi_1. \quad (80)$$

The scalar equations of motion to first order in perturbation can be written in the form

$$\delta\ddot{\chi}_1 + h_1\delta\chi_1 + h_2\delta\dot{\chi}_2 - (h_3\cos\eta_0 - h_4)\delta\ddot{\chi}_3 + h_5\sin\eta_0\delta\dot{\chi}_3 = 0, \quad (81)$$

$$\delta\ddot{\chi}_2 + h_1\delta\chi_2 - h_2\delta\dot{\chi}_1 + h_3\sin\eta_0\delta\ddot{\chi}_3 + (h_5\cos\eta_0 - h_6)\delta\dot{\chi}_3 = 0, \quad (82)$$

$$\delta\ddot{\chi}_3 + (h_7\cos\eta_0 - h_8)\delta\chi_1 - h_7\sin\eta_0\delta\chi_2 + h_9\sin\eta_0\delta\dot{\chi}_1 + (h_9\cos\eta_0 - h_{10})\delta\dot{\chi}_2 + h_{11}\sin\eta_0\delta\dot{\chi}_3 = 0, \quad (83)$$

where

$$h_1 \equiv \Omega_0(\beta_\parallel+\beta_p) - \omega_b^2\gamma_\parallel^{-2} - (\beta_\parallel+\beta_p)^2, \quad (84)$$

$$h_2 \equiv \Omega_0 - 2(\beta_\parallel+\beta_p), \quad (85)$$

$$h_3 \equiv \frac{\alpha_-}{(\beta_\parallel+\beta_p)}, \quad (86)$$

$$h_4 \equiv \frac{\alpha_+}{(\beta_\parallel+\beta_p)}, \quad (87)$$

$$h_5 \equiv \left\{\Omega_0 + 2\left[\omega_b^2\beta_\parallel - (\beta_\parallel+\beta_p)\right]\right\}h_3 - \Omega_1\lambda_-, \quad (88)$$

$$h_6 \equiv \left\{\Omega_0 + 2\left[\omega_b^2\beta_\parallel - (\beta_\parallel+\beta_p)\right]\right\}h_4 - \Omega_1\lambda_+, \quad (89)$$

$$h_7 \equiv \Omega_1(\beta_\parallel+\beta_p)\lambda_-, \quad (90)$$

$$h_8 \equiv \Omega_1(\beta_\parallel+\beta_p)\lambda_+, \quad (91)$$

$$h_9 \equiv \Omega_1\lambda_- - \omega_b^2\beta_\parallel h_3, \quad (92)$$

$$h_{10} \equiv \Omega_1\lambda_+ - \omega_b^2\beta_\parallel h_4, \quad (93)$$

$$h_{11} \equiv \frac{h_7h_4 - h_8h_3}{(\beta_\parallel+\beta_p)}. \quad (94)$$

The necessary condition for the stability of the electron orbits may be obtained by assuming that all perturbed quantities have the time variations as $\delta\chi_j = A_j\exp(i\omega\tau)$. Applying this condition to equations (81)–(83), we obtain three coupled homogeneous linear equations,

$$(h_1-\omega^2)A_1 + i\omega h_2A_2 + \left[i\omega h_5\sin\eta_0 + \omega^2(h_3\cos\eta_0 - h_4)\right]A_3 = 0, \quad (95)$$

$$(h_1-\omega^2)A_2 - i\omega h_2A_1 + \left[i\omega(h_5\cos\eta_0 - h_6) - \omega^2h_3\sin\eta_0\right]A_3 = 0, \quad (96)$$

$$\left[h_7\cos\eta_0 - h_8 + i\omega h_9\sin\eta_0\right]A_1 + \left[i\omega(h_9\cos\eta_0 - h_{10}) - h_7\sin\eta_0\right]A_2 + \left[i\omega h_{11}\sin\eta_0 - \omega^2\right]A_3 = 0. \quad (97)$$

Now, imposing the condition of a non-trivial solution for these equations and using the average over wavelength to eliminate rapid oscillations results a quadratic equation in ω^2,

$$\omega^4 - b\omega^2 + c = 0, \quad (98)$$

where

$$b \equiv 2h_1 + h_2^2 - h_5h_9 - h_6h_{10} + h_3h_7 + h_4h_8 + h_2(h_3h_9 + h_4h_{10}), \quad (99)$$

and

$$c \equiv h_1^2 + h_1(h_3h_7 + h_4h_8) + h_5(h_2h_7 - h_1h_9) + h_6(h_2h_8 - h_1h_{10}). \quad (100)$$

Therefore, the system will be stable if both roots of equation (98) in the characteristic equation are real and positive.

References

Ackermann, W. *et al.* (2007). *Nat. Photon.* **1**, 336–342.

Allaria, E., Appio, R., Badano, L., Barletta, W. A., Bassanese, S., Biedron, S. G., Borga, A., Busetto, E., Castronovo, D., Cinquegrana, P., Cleva, S., Cocco, D., Cornacchia, M., Craievich, P., Cudin, I., D'Auria, G., Dal Forno, M., Danailov, M. B., De Monte, R., De Ninno, G., Delgiusto, P., Demidovich, A., Di Mitri, S., Diviacco, B., Fabris, A., Fabris, R., Fawley, W., Ferianis, M., Ferrari, E., Ferry, S., Froehlich, L., Furlan, P., Gaio, G., Gelmetti, F., Giannessi, L., Giannini, M., Gobessi, R., Ivanov, R., Karantzoulis, E., Lonza, M., Lutman, A., Mahieu, B., Milloch, M., Milton, S. V., Musardo, M., Nikolov, I., Noe, S., Parmigiani, F., Penco, G., Petronio, M., Pivetta, L., Predonzani, M., Rossi, F., Rumiz, L., Salom, A., Scafuri, C., Serpico, C., Sigalotti, P., Spampinati, S., Spezzani, C., Svandrlik, M., Svetina, C., Tazzari, S., Trovo, M., Umer, R., Vascotto, A., Veronese, M., Visintini, R., Zaccaria, M., Zangrando, D. & Zangrando, M. (2012). *Nat. Photon.* **6**, 699–704.

Allaria, E., Badano, L., Bassanese, S., Capotondi, F., Castronovo, D., Cinquegrana, P., Danailov, M. B., D'Auria, G., Demidovich, A., De Monte, R., De Ninno, G., Di Mitri, S., Diviacco, B., Fawley, W. M., Ferianis, M., Ferrari, E., Gaio, G., Gauthier, D., Giannessi, L., Iazzourene, F., Kurdi, G., Mahne, N., Nikolov, I., Parmigiani, F., Penco, G., Raimondi, L., Rebernik, P., Rossi, F., Roussel, E., Scafuri, C., Serpico, C., Sigalotti, P., Spezzani, C., Svandrlik, M., Svetina, C., Trovó, M., Veronese, M., Zangrando, D. & Zangrando, M. (2015). *J. Synchrotron Rad.* **22**, 485–491.

Amann, J., Berg, W., Blank, V., Decker, F.-J., Ding, Y., Emma, P., Feng, Y., Frisch, J., Fritz, D., Hastings, J., Huang, Z., Krzywinski, J.,

Lindberg, R., Loos, H., Lutman, A., Nuhn, H.-D., Ratner, D., Rzepiela, J., Shu, D., Shvyd'ko, Y., Spampinati, S., Stoupin, S., Terentyev, S., Trakhtenberg, E., Walz, D., Welch, J., Wu, J., Zholents, A. & Zhu, D. (2012). *Nat. Photon.* **6**, 693–698.
Amri, H. E. & Mohsenpour, T. (2016). *Phys. Plasmas*, **23**, 022101.
Bacci, A., Ferrario, M., Maroli, C., Petrillo, V. & Serafini, L. (2006). *Phys. Rev.* **9**, 060704.
Bonifacio, R. (2005). *Nucl. Instrum. Methods Phys. Res. A*, **546**, 634–638.
Bonifacio, R. C., Pellegrini, C. & Narducci, L. M. (1984). *Opt. Commun.* **50**, 373–378.
Bonifacio, R. N., Piovella, N., Cola, M. M. & Volpe, L. (2007). *Nucl. Instrum. Methods Phys. Res. A*, **577**, 745–750.
Bourdier, A. & Michel-Lours, L. (1994). *Phys. Rev. E*, **49**, 3353–3359.
Dattoli, G., Di Palma, E., Petrillo, V., Rau, J. V., Sabia, E., Spassovsky, I., Biedron, S. G., Einstein, J. & Milton, S. V. (2015). *Nucl. Instrum. Methods Phys. Res. A*, **798**, 144–151.
Dattoli, G. V., Petrillo, V. & Rau, J. V. (2012). *Opt. Commun.* **285**, 5341–5346.
Dattoli, G., Renieri, A. & Torre, A. (1993). *Lectures on Free Electron Laser and Related Topics.* Singapore: World Scientific.
Dattoli, G. C., Retardi, C. & Vazquez, R. (1999). *Phys. Lett. A*, **257**, 26–30.
Freund, H. P. & Antonsen, T. M. Jr (1992). *Principles of Free-Electron Lasers.* London: Chapman and Hall.
Freund, H. P., Jackson, R. H. & Pershing, D. E. (1993). *Phys. Fluids B*, **5**, 2318.
Fuchs, M., Weingartner, R., Popp, A., Major, Z., Becker, S., Osterhoff, J., Cortrie, I., Zeitler, B., Hörlein, R., Tsakiris, G. D., Schramm, U., Rowlands-Rees, T. P., Hooker, S. M., Habs, D., Krausz, F., Karsch, S. & Grüner, F. (2009). *Nat. Phys.* **5**, 826–829.
Geloni, G., Kocharyan, V. & Saldin, E. (2011). *J. Mod. Opt.* **58**, 1391–1403.
Gordon, D. F., Sprangle, P., Hafizi, B. & Roberson, C. W. (2001). *Nucl. Instrum. Methods Phys. Res. A*, **475**, 190–194.
Grüner, F., Becker, S., Schramm, U., Eichner, T., Fuchs, M., Weingartner, R., Habs, D., Meyer-ter-Vehn, J., Geissler, M., Ferrario, M., Serafini, L., van der Geer, B., Backe, H., Lauth, W. & Reiche, S. (2007). *Appl. Phys. B*, **86**, 431–435.
Hafizi, B. & Roberson, C. W. (1996). *Nucl. Instrum. Methods Phys. Res. A*, **375**, 78–81.
Harmand, M., Coffee, R., Bionta, M. R., Chollet, M., French, D., Zhu, D., Fritz, D. M., Lemke, H. T., Medvedev, N., Ziaja, B., Toleikis, S. & Cammarata, M. (2013). *Nat. Photon.* **7**, 215–218.
Hasanbeigi, A. H., Mehdian, H. & Jafari, S. (2010). *Contrib. Plasma Phys.* **50**, 156–164.
Hedayati, R. S., Jafari, S. & Batebi, S. (2015). *Plasma Phys. Contrib. Fusion*, **57**, 085007.
Huang, Z. & Kim, K. J. (2007). *Phys. Rev. ST Accel. Beams*, **10**, 034801.
Ishikawa, T., Aoyagi, H., Asaka, T., Asano, Y., Azumi, N., Bizen, T., Ego, H., Fukami, K., Fukui, T., Furukawa, Y., Goto, S., Hanaki, H., Hara, T., Hasegawa, T., Hatsui, T., Higashiya, A., Hirono, T., Hosoda, N., Ishii, M., Inagaki, T., Inubushi, Y., Itoga, T., Joti, Y., Kago, M., Kameshima, T., Kimura, H., Kirihara, Y., Kiyomichi, A., Kobayashi, T., Kondo, C., Kudo, T., Maesaka, H., Maréchal, X. M., Masuda, T., Matsubara, S., Matsumoto, T., Matsushita, T., Matsui, S., Nagasono, M., Nariyama, N., Ohashi, H., Ohata, T., Ohshima, T., Ono, S., Otake, Y., Saji, C., Sakurai, T., Sato, T., Sawada, K., Seike, T., Shirasawa, K., Sugimoto, T., Suzuki, S., Takahashi, S., Takebe, H., Takeshita, K., Tamasaku, K., Tanaka, H., Tanaka, R., Tanaka, T., Togashi, T., Togawa, K., Tokuhisa, A., Tomizawa, H., Tono, K., Wu, S., Yabashi, M., Yamaga, M., Yamashita, A., Yanagida, K., Zhang, C., Shintake, T., Kitamura, H. & Kumagai, N. (2012). *Nat. Photon.* **6**, 540–544.
Jafari, S. F., Jafarinia, F., Nilkar, M. & Amiri, M. (2014). *Plasma Phys. Contrib. Fusion*, **56**, 125010.
Kawamura, Y. D., Li, D., Ruschin, S., Tanabe, T. & Toyoda, K. (2000). *Nucl. Instrum. Methods Phys. Res. A*, **445**, 241–246.
Kho, T. H. & Lin, A. T. (1988). *Int. J. Infrared Milli Waves*, **9**, 935–947.
Lehmkühler, F., Gutt, C., Fischer, B., Schroer, M., Sikorski, M., Song, S., Roseker, W., Glownia, J., Chollet, M., Nelson, S., Tono, K., Katayama, T., Yabashi, M., Ishikawa, T., Robert, A. & Grübel, G. (2014). *Sci. Rep.* **4**, 5234.
Margaritondo, G. & Rebernik Ribic, P. (2011). *J. Synchrotron Rad.* **18**, 101–108.
McNeil, B. W. J. & Thompson, N. R. (2010). *Nat. Photon.* **4**, 814–821.
Mehdian, H. S., Jafari, S. & Hasanbeigi, A. (2008). *Phys. Plasmas*, **15**, 073102.
Milton, S., Gluskin, E., Arnold, N. D., Benson, C., Berg, W., Biedron, S. G., Borland, M., Chae, Y. C., Dejus, R. J., Den Hartog, P. K., Deriy, B., Erdmann, M., Eidelman, Y. I., Hahne, M. W., Huang, Z., Kim, K. J., Lewellen, J. W., Li, Y., Lumpkin, A. H., Makarov, O., Moog, E. R., Nassiri, A., Sajaev, V., Soliday, R., Tieman, B. J., Trakhtenberg, E. M., Travish, G., Vasserman, I. B., Vinokurov, N. A., Wang, X. J., Wiemerslage, G. & Yang, B. X. (2001). *Science*, **292**, 2037–2041.
Mourou, G. & Tajima, T. (2011). *Opt. Photon. News*, **22**, 47.
Norby, R. J., DeLucia, E. H., Gielen, B., Calfapietra, C., Giardina, C. P., King, J. S., Ledford, J., McCarthy, H. R., Moore, D. J. P., Ceulemans, R., De Angelis, P., Finzi, A. C., Karnosky, D. F., Kubiske, M. E., Lukac, M., Pregitzer, K. S., Scarascia-Mugnozza, G. E., Schlesinger, W. H. & Oren, R. (2005). *Proc. Natl Acad. Sci. USA*, **102**, 18052–18056.
Olumi, M. B., Maraghechi, B. & Rouhani, M. H. (2011). *Plasma Phys. Contrib. Fusion*, **53**, 015010.
Parmigiani, F. & Ratner, D. (2016). *Synchrotron Radiat. News*, **29**, 2.
Petrillo, V. L., Serafini, L. & Tomassini, P. (2008). *Phys. Rev. ST Accel. Beams*, **11**, 070703.
Polyanskiy, M., Pogorelsky, I. V. & Yakimenko, V. (2011). *Opt. Express*, **19**, 7717–7725.
Ratner, D., Abela, R., Amann, J., Behrens, C., Bohler, D., Bouchard, G., Bostedt, C., Boyes, M., Chow, K., Cocco, D., Decker, F. J., Ding, Y., Eckman, C., Emma, P., Fairley, D., Feng, Y., Field, C., Flechsig, U., Gassner, G., Hastings, J., Heimann, P., Huang, Z., Kelez, N., Krzywinski, J., Loos, H., Lutman, A., Marinelli, A., Marcus, G., Maxwell, T., Montanez, P., Moeller, S., Morton, D., Nuhn, H. D., Rodes, N., Schlotter, W., Serkez, S., Stevens, T., Turner, J., Walz, D., Welch, J. & Wu, J. (2015). *Phys. Rev. Lett.* **114**, 054801.
Reiser, M. (1994). *Theory and Design of Charged Particle Beams.* New York: Wiley.
Ribic, P. R. & Margaritondo, G. (2012). *J. Phys. D*, **45**, 213001.
Sprangle, P. B., Hafizi, B. & Penano, J. R. (2009). *Phys. Rev. ST Accel. Beams*, **12**, 050702.
Svitozar, S. (2016). *Synchrotron Radiat. News*, **29**, 10.
Svitozar, S., Krzywinski, J., Ding, Y. & Huang, Z. (2015). *Phys. Rev. ST Accel. Beams*, **18**, 030708.
Tiedtke, K., Azima, A., von Bargen, N., Bittner, L., Bonfigt, S., Düsterer, S., Faatz, B., Frühling, U., Gensch, M., Gerth, C., Guerassimova, N., Hahn, U., Hans, T., Hesse, M., Honkavaar, K., Jastrow, U., Juranic, P., Kapitzki, S., Keitel, B., Kracht, T., Kuhlmann, M., Li, W. B., Martins, M., Núñez, T., Plönjes, E., Redlin, H., Saldin, E. L., Schneidmiller, E. A., Schneider, J. R., Schreiber, S., Stojanovic, N., Tavella, F., Toleikis, S., Treusch, R., Weigelt, H., Wellhöfer, M., Wabnitz, H., Yurkov, M. V. & Feldhaus, J. (2009). *New J. Phys.* **11**, 023029.
Wu, J., Marinelli, A. & Pellegrini, C. (2012). *Proceedings of FEL2012*, Nara, Japan.
Yabashi, M., Tanaka, H. & Ishikawa, T. (2015). *J. Synchrotron Rad.* **22**, 477–484.
Yanovsky, V., Chvykov, V., Kalinchenko, G., Rousseau, P., Planchon, T., Matsuoka, T., Maksimchuk, A., Nees, J., Cheriaux, G., Mourou, G. & Krushelnick, K. (2008). *Opt. Express*, **16**, 2109–2114.
Zholents, A. A. (2005). *Phys. Rev. ST Accel. Beams*, **8**, 040701.